Chapter 5

A candidate for rotation-regulated massive star formation: S255IR–SMA1

K.-S. Wang, M. R. Hogerheijde, F. F. S. van der Tak, and P. D. Klaassen
submitted to A&A

Abstract

Context. It is poorly understood how massive stars form and whether accretion through a disk plays an important role. To study the accretion processes of the innermost regions of massive star-forming cores, high angular resolution observations in appropriate molecular line tracers are required.
Aims. Through subarcsecond resolution observations, we study the kinematics of the equatorial region of a massive star-forming core.
Methods. We observed the massive star forming region S255IR with the expanded Submillimeter Array (eSMA = SMA + JCMT + CSO 10.4m) at $\sim 0.3''$ resolution in a number of molecular lines as well as the continuum at 345 GHz.
Results. The 345-GHz continuum emission reveals a dense (10^9 cm^{-3}) disk-like structure around S255IR–SMA1. Two velocity components are identified with one ($V_{\rm LSR} \sim 4$ km s^{-1}) exclusively showing emission from hot core molecules around the forming massive star S255IR–SMA1. The component at $V_{\rm LSR} \sim 9$ km s^{-1} likely represents the large scale structure surrounding gas of SMA1 and SMA2. Optically thick CH_3OH lines show a clear velocity gradient roughly perpendicular to the reported jet/maser/outflow emission, implying a rotating disk-like structure. However, the velocities are not Keplerian for the expected stellar mass, but either solid body or subKeplerian with significant turbulence. From accretion luminosity analysis and a comparison of the derived high CH_3OH abundance ($X \sim 10^{-6}$) with chemical models, we suggest that the dynamical age of S255IR–SMA1 is small (10^{3-4} yrs; $> 10\times$ the local free-fall time). The accretion rate is a few times 10^{-5} to a few times 10^{-4} $M_\odot$ yr^{-1}.

Conclusions. We suggest that S255IR–SMA1 is a good candidate for massive star formation regulated a rotating, non-Keplerian structure. This structure is likely responsible for transporting gas from the outer envelope to the star. The actual Keplerian disk may hidden within 330 AU and requires at least $0.03''$ resolution observations in optically thin lines to properly resolve the disk kinematics in the equatorial plane of S255IR–SMA1.

5.1 Introduction

Disks and outflows are ubiquitous phenomena during the formation of low-mass stars ($M_\star \sim 1 M_\odot$, Shu et al. 1987). The forming star obtains its mass through accretion from the collapsing envelope to the circumstellar disk and further from the circumstellar disk to the star, while excess angular momentum can be transported away via the bipolar outflow. A similar formation scenario ("turbulent core accretion") has been proposed for the formation of higher-mass stars ($M_\star \approx 8 M_\odot$, McKee & Tan 2003). The high detection rate of collimated outflows in high-mass star-forming regions (Zhang et al. 2001; Beuther et al. 2002) implies that circumstellar disks may also be common in high-mass star formation, and supports the idea that a scaled-up version of low-mass star formation may be applicable to the formation of higher-mass stars. However, the rare detections of "disks" in high-mass star-forming cores to date (Cesaroni et al. 2007; Kraus et al. 2010; Beuther et al. 2012; Sánchez-Monge et al. 2013) may imply a different formation mechanism for high-mass stars (Zinnecker & Yorke 2007), such as "competitive accretion" in a clustered environment (Bonnell et al. 2001; Pillai et al. 2011). To test different ideas of high-mass star formation, it is therefore essential to study the innermost parts of high-mass star-forming cores to infer accretion signatures at high-angular resolution.

The existence of accretion disks around massive young stars has been shown with varying degrees of confidence around a few objects (Cesaroni et al. 2007). For young B-type stars, the disks are found to be large ($\sim 10^{2-4}$ AU) and massive ($M_{\rm disk} \leq M_\star$), which is quite different from the disks around low-mass stars ($M_{\rm disk} \ll M_\star$). On the other hand, only large toroids undergoing solid-body rotation (appearing as linear features in position-velocity plots) with masses greater than stellar masses are found toward young O-type stars (Furuya et al. 2008; Beltrán et al. 2011). In all cases, the key evidence rests on the presence of velocity gradients (roughly) orthogonal to the direction of large scale outflows. However, this kinematical evidence needs to be interpreted with caution, since unresolved multiplicity, chemical gradients, and the effects of small-scale outflows can conspire to produce a signature masquerading as a velocity gradient of a disk around a single source (e.g., Comito et al. 2007).

In this paper, we present sub-arcsecond resolution observations of the high-mass star-forming cluster S255IR, located between two evolved HII regions S255 and S257 (Sharpless 1959). From the measurements of maser parallaxes, Rygl et al. (2010) estimated a distance of $1.59^{+0.07}_{-0.06}$ kpc. The total bolometric luminosity at 1.6 kpc is about 2×10^4 $L_\odot$ (corresponding to an single early B-type star), derived from a spectral energy distribution fit (Minier et al. 2005). The adopted luminosity is consistent with the ones derived by Jaffe et al. (1984) and Mezger et al. (1988) within a factor of few. Near the central region of S255IR, Y. Wang et al. (2011) reported two major continuum emission peaks (SMA1 and SMA2) and one blended emission peak (SMA3) at 1.3 mm. A similar continuum map at 1.1 mm is also observed by Zinchenko et al. (2012) with an additional peak (SMA4) $10''$ to the south of SMA1. Among these four sources, only SMA1 is associated with cm-wave emission with a spectral index corresponding to an optically thin HII region (also known as S255-2c, Snell & Bally 1986; Rengarajan & Ho 1996; Ojha et al. 2011). SMA1 is very likely forming a massive star, while the others may be forming low- to intermediate-mass stars. In this paper, we assume that the total bolometric luminosity is associated exclusively with SMA1 for simplicity. We expect that the error of the true bolometric luminosity of SMA1 is much less than a factor of 2.

Outflow signatures in S255IR are observed with different tracers. The CO 2–1 maps presented by Y. Wang et al. (2011) show a jet-like outflow in the NE–SW direction on $40''$ scales. The same maps also indicate that there may be another outflow in the NW–SE direction on $10''$ scales. At 2.2 μm, Tamura et al. (1991) observed an extended NE–SW bipolar signature using scattered light (about $20''$ in size) together with a cluster of point sources, among which NIRS 1 (corresponding to SMA3) and NIRS 3 (corresponding to SMA1) are proposed to be associated with the bipolar feature. From their 2 μm polarimetric observations, Simpson et al. (2009) further suggest that SMA1 (NIRS 3) may be the driving source of the NE–SW bipolar feature, while SMA3 (NIRS 1) may be the driving source of a smaller bipolar feature in the N–S direction (about $10''$ in size). The NE–SW bipolar feature can be seen in Brγ emission on $\sim 20''$ scales, H_2 line emission on $\sim 30''$ scales and H_2O maser emission at subarcsecond scales with a position angle of about 67°, which traces shock activity from the jet or outflow originating from SMA1 (Howard et al. 1997; Miralles et al. 1997; Goddi et al. 2007). It is likely that the jet-like CO outflow in the NE-SW direction (Y. Wang et al. 2011) is correlated with the features seen at infrared and radio wavelengths. Based on this disk-outflow geometry, SMA1 is a promising target for the search for disk signatures. Interestingly, there is a velocity gradient roughly perpendicular to the NE-SW outflow observed in CH_3CN and $HCOOCH_3$ lines on $\sim 2''$ scales (Y. Wang et al. 2011), although the emission is barely resolved. Certainly, high angular resolution observations are required to further investigate the nature of the massive disk target SMA1.

In Sect. 5.2, we present our sub-arcsecond eSMA observations and data reduction. Observational results and data analysis are reported in Sect. 5.3, while discussions are presented in Sect. 5.4. We summarize our work in Sect. 5.5.

5.2 Observations

The expanded Submillimeter Array (eSMA) project (Bottinelli et al. 2008) combines the Submillimeter Array (SMA[1]), the James Clerk Maxwell Telescope (JCMT[2]), and the Caltech Submillimeter Observatory (CSO[3]) telescope as a single interferometer, which aims to enhance the sensitivity of the most extended SMA configuration in the 345-GHz band (Bottinelli et al. 2008). As part of science verification, S255IR was observed on February 10, 2010 with the SMA (7 antennas) and the JCMT only, resulting in uv sampling ranging from 100 kλ ($2''$) to 700 kλ ($0.3''$) at 345 GHz. The phase center was $\alpha(2000) = 06^{\rm h}12^{\rm m}54\overset{\rm s}{.}00$, $\delta(2000) = 17^\circ59'23\overset{''}{.}0$. The total on-source time is about 4 hours. A single spectral setup to observe CO $J = 3-2$ at 345.796 GHz was adopted. With this setup, we were able to observe the continuum at 345 GHz as well as some molecular lines within the total 4-GHz bandwidth ($334.2 - 336.2$ GHz and $344.2 - 346.2$ GHz; see Sect. 5.3). We adopted 128 channels to sample each spectral window, resulting in a velocity resolution of 0.7 km s^{-1}. The quasars 0532+075 ($\sim$0.4 Jy; 14° away) and 0750+125 ($\sim$1.0 Jy; 24° away) were observed every 15 minutes for gain calibration. 3C273 was observed for passband calibration. Pallas (1.0 Jy) was adopted as the flux reference. We estimate the absolute flux uncertainty to be about 20%.

Data reduction was conducted by using the MIR package (Scoville et al. 1993) adapted for the SMA, while imaging and analysis were performed in MIRIAD (Sault et al. 1995). The phases of the continuum visibilities were self-calibrated by selecting the brightest clean components as the model. We applied natural weighting to both continuum and line data for best sensitivity. Line identification was conducted with the aid of molecular spectroscopy databases of JPL[4] (Pickett et al. 1998) and CDMS[5] (Müller et al. 2005).

[1]The Submillimeter Array is a joint project between the Smithsonian Astrophysical Observatory and the Academia Sinica Institute of Astronomy and Astrophysics and is funded by the Smithsonian Institution and the Academia Sinica.

[2]The James Clerk Maxwell Telescope is operated by the Joint Astronomy Centre on behalf of the Science and Technology Facilities Council of the United Kingdom, the National Research Council of Canada, and (until 31 March 2013) the Netherlands Organisation for Scientific Research.

[3]Caltech Submillimeter Observatory is operated by the California Institute of Technology under cooperative agreement with the National Science Foundation (AST-0838261).

[4]http://spec.jpl.nasa.gov/

[5]http://www.astro.uni-koeln.de/cdms/

5.3 Results and analysis

5.3.1 Continumm emission at 345 GHz

Figure 5.1 shows the images and vector-averaged visibilities of the continuum emission at 345 GHz. The target source S255IR–SMA1 is resolved by the eSMA. We derive the source size in the visibility domain by assuming a Gaussian geometry. The deconvolved source size for SMA1 is $0\farcs23 \times 0\farcs19$ ($\sim$ 370 AU $\times$ 300 AU at $d = 1.6$ kpc) with P.A. of -29° (Table 5.1). Although the aspect ratio ($\sim$0.8) is close to unity, the position angle implies that the continuum emission may trace a flattened structure roughly perpendicular to the large scale CO outflow with P.A. $\sim 65^\circ$ (Y. Wang et al. 2011). From the visibility modeling of the peak position of SMA1, we found an offset $\sim 0.08''$ to the south-east direction relative to the position derived from the SMA 1.3mm observations (Table 5.1; Y. Wang et al. 2011). The offset may be real, or due the phase error since the adopted phase calibrators are faint and no so close to the target (Sect. 5.2), or due to the self-calibration process.

The other mm-wave sources, SMA2 and SMA3 reported by Y. Wang et al. (2011), are not detected at the 1-σ level (2.4 mJy beam^{-1}). SMA4 observed by Zinchenko et al. (2012) is outside our field of view. The non-detection of SMA2 and SMA3 is likely due to the spatial filtering of the eSMA observations. The array is not sensitive to structures larger than $2''$. From SMA observations of S255IR at 1.3 mm, Y. Wang et al. (2011) reported peak flux densities of SMA1, SMA2 and SMA3 of 95, 52 and 30 mJy beam^{-1} (beam size $\sim 2''$), respectively. Assuming all the sources have the same spectral index and source size, our detected peak flux density of 179 mJy of SMA1 at 345 GHz implies that the peak flux density of SMA2 and SMA3 at 345 GHz should be 98 and 57 mJy beam^{-1}, respectively, which should be detected with an S/N of at least 24. From the SMA 1.3 mm continuum image (Y. Wang et al. 2011), the emission toward SMA1 is compact and centrally peaked, while SMA2 is resolved with the $\sim 2''$ beam and less centrally peaked. The weaker and diffuse emission from SMA3 is likely from the common envelope of SMA1 and SMA2. Therefore, we suggest that the continuum emission of SMA2 and SMA3 at 345 GHz is likely resolved out by the eSMA.

5.3.1.1 H_2 mass and column density

From the measured 345-GHz continuum, we estimate the H_2 mass and H_2 column density toward S255IR–SMA1. Assuming optically thin emission, the H_2 column density at the emission peak can be estimated via

$$N(\mathrm{H_2}) = \frac{I_\nu a}{2 m_\mathrm{H} \Omega_b \kappa_\nu B_\nu(T_\mathrm{d})}, \tag{5.1}$$

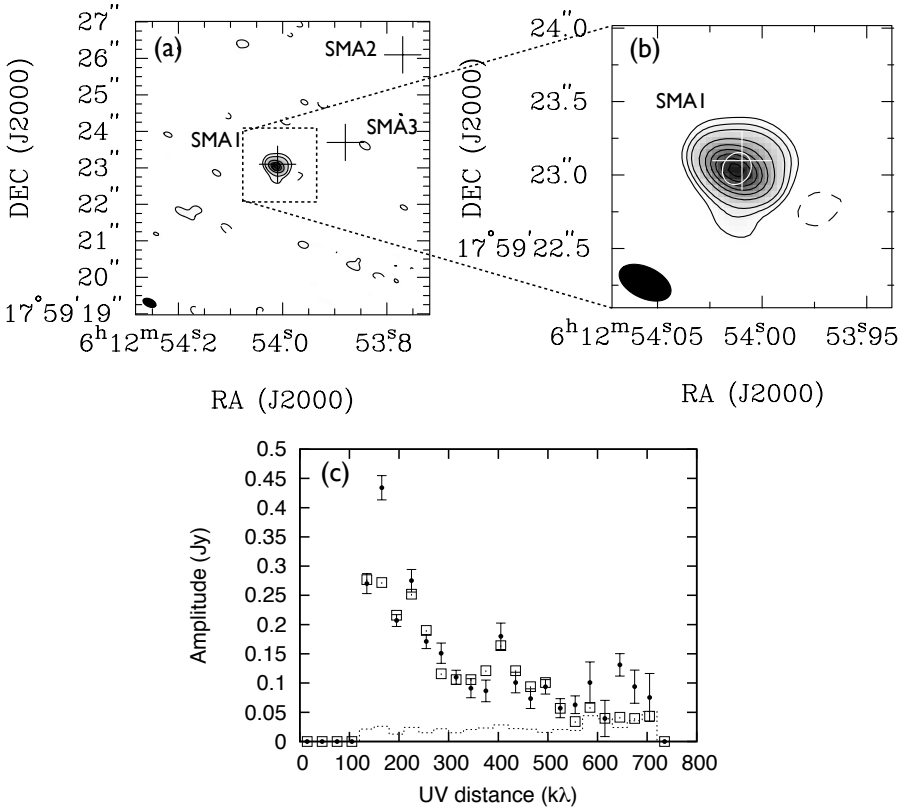

Figure 5.1 (a) Continuum image of S255IR at 345 GHz. Natural weighting is applied, resulting a clean beam size of $0.38'' \times 0.21''$, P.A. 65° (filled ellipse at bottom-left corner). Contour levels are -3, 3, 10, 30, 50, and 70 σ with 1-σ noise level of 2.4 mJy beam^{-1}. The peak intensity is 179 mJy beam^{-1}. The positions of the continuum sources SMA1, SMA2 and SMA3 detected by Y. Wang et al. (2011) are marked as crosses. The sources SMA2 and SMA3 are not detected at 1-σ noise level. (b) Continuum image of S255IR–SMA1 at 345 GHz. Contour levels are -3, 3, 6, 10, 20, 30, 40, 50, 60 and 70 σ with 1-σ noise level of 2.4 mJy beam^{-1}. The white cross is the peak position derived from the SMA observations at 1.3 mm. The white ellipse represents the source FWHM size derived from the visibility fit. The best-fit source FWHM size is $0.23''$ ($\sim$370 AU) by $0.19''$ ($\sim$300 AU) with P.A. -29°. (c) Vector-averaged visibilities of the continuum emission at 345 GHz. The observed data are shown as filled circles with error bars and the model fit with a Gaussian is shown as open squares. The dotted histogram represents the zero-intensity values.

Table 5.1. Physical properties of the 345 GHz continuum in S255IR

Component	RA(J2000) (h m s)	Dec(J2000) (° ′ ″)	$\theta_{\rm maj}{}^a$ (″)	$\theta_{\rm min}{}^a$ (″)	P.A.^{a} (°)	$I_\nu{}^b$ (mJy beam^{-1})	$S_\nu{}^c$ (Jy)	$N(\mathrm{H_2})^b$ ($\times 10^{24}$ cm^{-2})	$M(\mathrm{H_2})^c$ ($M_\odot$)	$n(\mathrm{H_2})^c$ ($\times 10^9$ cm^{-3})
SMA1^{d,e}	06 12 54.01	17 59 23.1	0.23	0.19	-29	179	0.30	2.5	0.36	3.4
SMA2^e	06 12 53.77	17 59 26.1	...	...	...	< 2.4	...	< 0.03	...	...
SMA3^e	06 12 53.88	17 59 23.7	...	...	...	< 2.4	...	< 0.03	...	...

Note. — ^{a}Gaussian FWHM size and position angle. ^{b}Peak intensity and beam-averaged H_2 column density assuming $T_{\rm dust} = 140$ K. 1-σ upper limit is given for SMA2 and SMA3. We note that our dataset is not sensitive to scales greater than $\sim 2''$ (100 kλ). The emission from SMA2 and SMA3 is likely filtered out. ^{c}Integrated flux density, H_2 mass and H_2 volume density. We assume $T_{\rm dust} = 140$ K. The values are calculated assuming a distance of 1.6 kpc. If the distance is not 1.6 kpc, $M(\mathrm{H_2})$ and $n(\mathrm{H_2})$ are scaled as 0.36(d/1.6 kpc)^2 $M_\odot$ and 3.4(d/1.6 kpc)$^{-1}$ cm^{-3}, respectively. ^{d}The peak position derived from the visibility fit is RA(J2000) = $06^{\rm h}12^{\rm m}54\overset{\rm s}{.}012$, Dec(J2000) = $17^\circ 59' 23\overset{''}{.}05$. ^{e}The listed positions are adopted from Y. Wang et al. (2011).

where I_ν is the peak flux density, a is the gas-to-dust ratio (100), Ω_b is the beam solid angle, $m_{\rm H}$ is the mass of atomic hydrogen, κ_ν is the dust opacity per unit mass and $B_\nu(T_{\rm d})$ is the Planck function at dust temperature $T_{\rm d}$ (Hildebrand 1983). We apply the interpolated value of $\kappa_\nu(870\mu{\rm m}) \approx 2.1$ cm^2 g^{-1} as suggested by Ossenkopf & Henning (1994) for gas densities of $10^6 - 10^8$ cm^{-3} and coagulated dust particles with thin ice mantles. The dust temperature is assumed to be 140 K (see excitation analysis, Sect. 5.3.2.2). The H_2 mass is estimated from the total flux density derived from the visibility fit (Table 5.1) via

$$M({\rm H_2}) = \frac{S_\nu d^2 a}{\kappa_\nu B_\nu(T_{\rm d})}, \tag{5.2}$$

where S_ν is the total flux density of dust emission and d (1.6 kpc) is the distance to the source (Hildebrand 1983). Assuming a spherical source with 330 AU in diameter (geometric mean of the decomposed size), the H_2 number density is also derived. The calculations of $N_{\rm H_2}$ and $M_{\rm H_2}$ are not corrected for any contribution of free-free emission at 345 GHz. The VLA measurement of free-free emission at 15 GHz is 3.1 mJy (Ojha et al. 2011). The extrapolated optically thin free-free emission at 345 GHz is 2.3 mJy, which is only 0.8% of the total flux density at 345 GHz. Therefore, the free-free emission at 345 GHz can be ignored. We summarized these results in Table 5.1. Toward S255IR–SMA1, we find that the beam-averaged H_2 column density is $\sim 2.5 \times 10^{24}$ cm^{-2}. The H_2 mass is 0.36 $M_\odot$. This is only a few percent of the stellar mass expected for an early B-type star. A high H_2 number density of $\sim 3.4 \times 10^9$ cm^{-3} is derived. If the assumed dust temperature has an uncertainty of a factor of 2, the derived quantities have a factor of 2 in uncertainty. We expect that a significant amount of the continuum flux is missing due to the limited short spacing data of the eSMA, therefore the derived quantities should be treated as lower limits. It is because of this spatial filtering that we can study the dense environment of S255IR down to few hundred AU scales for the first time without the contamination from structures at thousand AU scales.

5.3.2 Molecular line emission

The 4-GHz bandwidth of the eSMA allows us to observe several molecular lines including simple molecules (CO, SO, SO_2, $H^{13}CN$ and HCCCN) as well as hot-core molecules (HCOOH, CH_3OH and NH_2CHO). All of our detected species and transitions are summarized in Table 5.2.

5.3.2.1 Molecular images and spectra

In Fig. 5.2, we present the molecular gas distributions of S255IR–SMA1 and the individual spectra taken at the continuum peak position. We do not image

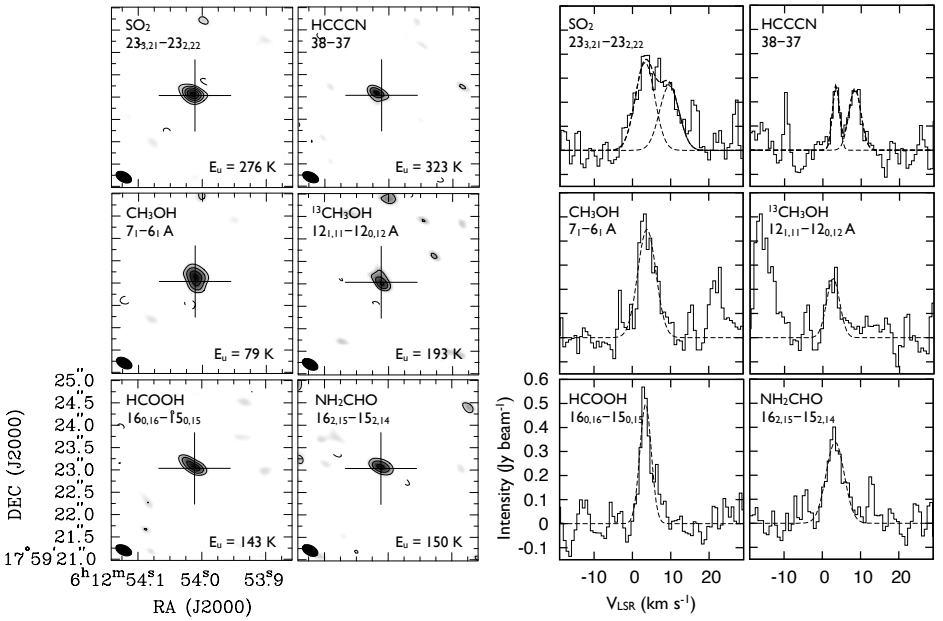

Figure 5.2 (Left) Sample zero moment maps of molecular species toward S255IR–SMA1. The cross represents the peak position of the continuum emission derived from our data. The typical angular resolution is $0\farcs38 \times 0\farcs22$, P.A. 63°. The contour levels are -3, 3, 5, 7,...σ for all the molecules except $^{13}CH_3OH$ that the contours are -3,3,4,5...σ. The 1-σ noise levels for SO_2, HCCCN, CH_3OH, $^{13}CH_3OH$, HCOOH and NH_2CHO are 0.40, 0.28, 0.34, 0.22, 0.25 and 0.28 Jy beam^{-1} km s^{-1}, respectively. (Right) The beam averaged spectra taken at the position of the continuum peak. The species are identical to the maps shown in the left panels. The dashed lines represent the Gaussian fit of the spectra. The fitting results are summarized in Table 5.2.

the CO $J = 3 - 2$ emission due to the missing flux (expected $> 90\%$; Sect. 5.2). SO $8_8 - 7_7$ is blended with CH_3OH at 344.312 GHz and $H^{13}CN$ $J = 4 - 3$ is blended with SO_2 at 345.338 GHz. Therefore, we do not show their images in Fig. 5.2. For the other species, we found that the emission is compact and near the position of the continuum peak: CH_3OH $7_1 - 6_1$ A is resolved, and SO_2 $23_{3,21} - 23_{2,22}$ is barely resolved. Other species are unresolved. Our results suggest that S255IR–SMA1 contains active hot-core chemistry because we detect compact emission from complex organic molecules which are also observed by Y. Wang et al. (2011) and Zinchenko et al. (2012).

Table 5.2. Detected molecular lines in S255IR–SMA1

Molecule	Frequency (MHz)	Transition	E_u[a] (K)	V_{LSR}[b] (km s^{-1})	ΔV[c] (km s^{-1})	$\int I_\nu dV$[d] (Jy beam^{-1} km s^{-1})	Note
			1st velocity component				
CO	345795.990	3–2	33	...	...	...	Not imaged.
SO	344310.612	8_8–7_7	87	3.8 (fixed)	8.9 ± 1.3	2.35 ± 0.44	b[e]:CH_3OH(344312)
$H^{13}CN$	345339.760	4–3	41	~ 3.4	~ 4.9	...	b[e]:SO_2(345338)
SO_2	334673.352	$8_{2,6}$–$7_{1,7}$	43	5.7 ± 0.8	13.3 ± 1.8	2.86 ± 0.33	single line fit, 2σ detection
	336089.226	$23_{3,21}$–$23_{2,22}$	276	3.3 ± 0.4	6.0 (fixed)	2.33 ± 0.21	
	345338.539	$13_{2,12}$–$12_{1,11}$	93	~ 3.4	~ 4.9	...	b[e]:$H^{13}CN$(345339)
HCCCN	345609.010	38–37	323	3.4 ± 0.2	2.1 ± 0.5	0.61 ± 0.13	
HCOOH	334265.827	$15_{2,14}$–$14_{2,13}$	142	2.8 ± 0.2	3.5 ± 0.7	1.89 ± 0.14	
	345030.596	$16_{0,16}$–$15_{0,15}$	143	3.4 ± 0.1	3.5 ± 0.3	1.86 ± 0.15	
CH_3OH	334426.571	3_0–2_1 $E, v_t = 1$	314	4.6 ± 0.6	6.6 ± 1.5	0.82 ± 0.16	
	335133.570	2_2–3_1 A	45	3.6 ± 0.2	3.1 ± 0.4	1.36 ± 0.14	
	335582.017	7_1–6_1 A	79	3.8 ± 0.2	5.6 ± 0.5	2.67 ± 0.22	
	344312.267	10_{-2}–11_{-3} $E, v_t = 1$	492	3.8 (fixed)	4.9 (fixed)	1.69 ± 0.30	b[e]:SO(344310)
	344443.433	19_1–18_2 A	451	4.0 ± 0.2	3.7 ± 0.4	1.53 ± 0.14	
	345903.916	16_1–15_2 A	333	2.7 ± 0.3	5.0 ± 0.7	2.42 ± 0.31	
	345919.260	18_{-3}–17_{-4} E	459	4.0 ± 0.5	5.3 ± 1.1	2.13 ± 0.38	
$^{13}CH_3OH$	335560.207	$12_{1,11}$–$12_{0,12}$ A	193	2.7 ± 0.3	4.0 ± 0.6	1.05 ± 0.15	
NH_2CHO	336136.877	$16_{2,15}$–$15_{2,14}$	150	3.4 ± 0.4	5.6 ± 1.0	2.02 ± 0.30	
	345182.618	$17_{0,17}$–$16_{0,16}$	152	3.7 ± 0.2	3.7 ± 0.4	2.09 ± 0.19	
	345326.689	$16_{1,15}$–$15_{1,14}$	145	3.3 ± 0.4	5.3 ± 0.9	2.52 ± 0.43	partially b[e]:SO_2(345338)

Table 5.2 (cont'd)

Molecule	Frequency (MHz)	Transition	E_u [a] (K)	V_{LSR} [b] (km s^{-1})	ΔV [c] (km s^{-1})	$\int I_\nu dV$ [d] (Jy beam^{-1} km s^{-1})	Note
2nd velocity component							
SO	344310.612	8_8–7_7	87	10.6 ± 0.2	3.3 ± 0.4	1.26 ± 0.18	
$H^{13}CN$	345339.760	4–3	41	~ 8.7	~ 4.2	...	b[e]:SO_2(345338)
SO_2	336089.226	$23_{3,21}$–$23_{2,22}$	276	9.6 ± 0.5	6.0 (fixed)	1.72 ± 0.21	
	345338.539	$13_{2,12}$–$12_{1,11}$	93	~ 8.7	~ 4.2	...	b[e]:$H^{13}CN$(345339)
HCCCN	345609.010	38–37	323	8.3 ± 0.3	3.7 ± 0.7	1.01 ± 0.17	

Note. — [a]Upper level energy. [b]Line center velocity. The formal fitting errors are given, however, the channel resolution is $\sim$ 0.7 km s^{-1}. [c]FWHM line width. The formal fitting errors are given, however, the channel resolution is $\sim$ 0.7 km s^{-1}. [d]Integrated line intensity. The formal fitting errors are given. The absolute flux error ($\sim 20\%$) is not considered. [e]Line blending.

Although spatially the distributions of the molecules presented in Fig. 5.2 (Left) are similar, in the velocity domain these species show significant differences (Fig. 5.2, Right). To quantify the line profiles, we applied Gaussian line profile fits to all the imaged molecules and transitions. The results are summarized in Table 5.2. For simple molecules such as SO_2 and HCCCN, the lines appear wider than the hot-core molecules (e.g., CH_3OH, HCOOH and NH_2CHO). A significant difference in LSR velocity also exists between these two groups of molecules. The HCCCN $J = 38 - 37$ spectrum shows that the line profile may be double-peaked. The double-peaked line profile can be seen much more clearly in the SO $8_8 - 7_7$ and the $H^{13}CN$ $J = 4 - 3$ spectra although these two line profiles are contaminated by other molecules (Fig. 5.3). We suggest that the double-peaked line profile is likely real since the depth of the dip is significantly greater than the noise level. We assume that the double-peaked profile is a combination of two different velocity components. To fit the SO line profile, we assumed that the LSR velocity of CH_3OH $10_{-2} - 11_{-3}$ $Ev_t = 1$ is fixed to the mean value (3.8 km s^{-1}) derived from other isolated CH_3OH lines. To fit the blended $H^{13}CN/SO_2$ line profile, only one set of double-peaked profile is used since the difference of the rest frequencies of the two lines is small ($\sim$ 1 km s^{-1}).

Our eSMA data show that there are two velocity components around S255IR–SMA1: a "blue-shifted" one at mean LSR velocity of 3.6 km s^{-1} and a "red-shifted" one at mean LSR velocity of 9.2 km s^{-1}. These two components are different in chemical point of view. The "blue-shifted" component contains both simple molecules and hot-core molecules, while the "red-shifted" component only shows the emission from simple molecules. Y. Wang et al. (2011) reported that the LSR velocity of ^{13}CO $J = 2 - 1$ from the IRAM 30m telescope (7.7 km s^{-1}) is different from the velocity measured by the SMA based on CH_3CN (5.2 km s^{-1}). From NH_3 observations, Zinchenko et al. (2012) reported a LSR velocity of 4.4 km s^{-1}. Combining all the observational results, we suggest that the hot-core species are concentrated in a compact and dense region while the simple molecules are widely distributed (and observed in both velocity components). The nature of the difference in LSR velocities of the two groups, however, is not clear. The $C^{18}O$ 2–1 velocity map presented by Y. Wang et al. (2011) shows a clear velocity gradient from SMA1 ($V_{\rm LSR} \sim 5$ km s^{-1}) to SMA2 ($V_{\rm LSR} \sim 9$ km s^{-1}) and this velocity gradient can be modeled as Keplerian rotation. Likely, $C^{18}O$ 2–1 traces the common envelope of the binary SMA1 and SMA2, which has a higher mean LSR velocity. In this case, the widely distributed simple molecules are more affected by the interaction of SMA1 and SMA2, while the compact hot-core molecules are less affected by SMA2 and therefore can represent the true systemic velocity of S255IR–SMA1.

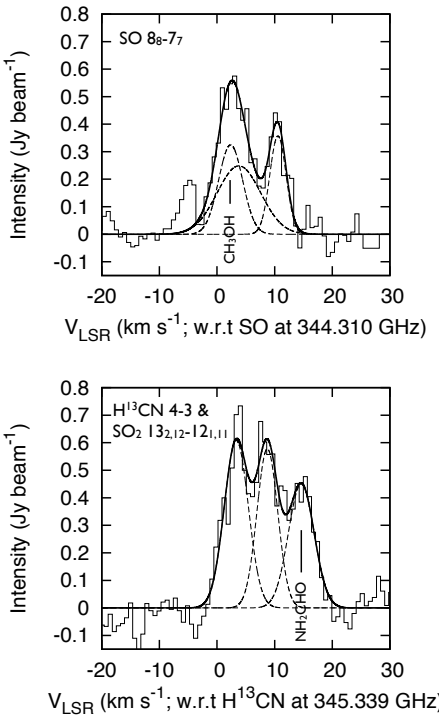

Figure 5.3 Blended line profiles of SO $8_8 - 7_7$ and $H^{13}CN$ $J = 4 - 3$ plus SO_2 $13_{2,12} - 12_{1,11}$. The dashed lines represent the Gaussian fit of individual components, while the solid lines are the synthetic spectra.

5.3.2.2 Excitation analysis

The detected seven transitions of CH_3OH allow us to perform excitation analysis toward S255IR–SMA1. We adopted the "population diagram" method described by Goldsmith & Langer (1999). The observed intensity of a given transition of CH_3OH can be transformed to the upper state column density per upper state statistical weight in logarithmic scale via

$$\ln(\frac{N_{\rm u}^{\rm obs}}{g_{\rm u}}) = \ln(\frac{2.04 \times 10^{20}}{\theta_a \theta_b} \frac{W}{g_I g_K \nu_0^3 S \mu_0^2}) \ {\rm cm}^{-2}, \tag{5.3}$$

where θ_a and θ_b are the major and minor axes of the clean beam in arcsec, respectively, W is the integrated intensity in Jy beam^{-1} km s^{-1}, g_I and g_K are the spin and projected rotational degeneracies, respectively, ν_0 is the rest frequency in GHz, S is the line strength and μ_0 is the dipole moment of the transition in Debye. Assuming that the level populations of CH_3OH follow a Boltzmann distribution at a single excitation temperature $T_{\rm ex}$, the left hand side of Eq. 5.3 can

be modeled as

$$\ln(\frac{N_{\rm u}^{\rm model}}{g_{\rm u}}) = \ln(\frac{N_{\rm tot}}{Q}) - \frac{E_{\rm u}}{kT_{\rm ex}} - \ln C_\tau + \ln f, \tag{5.4}$$

where $N_{\rm tot}$ is the total column density, Q is the partition function, $E_{\rm u}$ is the upper state energy, k is the Boltzmann constant, C_τ ($= \tau/1 - e^{-\tau}$) is the correction term of line opacity, and f is the beam filling factor ($\leq$ 1). The line center opacity assuming a Gaussian line profile is

$$\tau = \frac{c^3}{8\pi\nu_0^3}\frac{A_{\rm ul}}{\Delta V}\frac{g_u N_{\rm tot}}{Q}e^{-E_{\rm u}/kT_{\rm ex}}(e^{h\nu_0/T_{\rm ex}} - 1), \tag{5.5}$$

where c is the speed of light, $A_{\rm ul}$ the Einstein-A coefficient, ΔV is the FWHM line width, and h is the Planck constant. For a given set of $T_{\rm ex}$, $N_{\rm tot}$ and f, the left hand side of Eq. 5.4 can be calculated and compared with the left hand side of Eq. 5.3. We perform χ^2 minimization to search for a best-fit model. In Fig. 5.4, we plot the logarithm of the column densities from our data (Eq. 5.3) versus $E_{\rm u}$ (Eq. 5.4) as the red circles. The best-fit model is overplotted as the blue crosses. From this simple analysis, we found that all the CH_3OH transitions have opacities close or greater than unity. The excitation temperature is 140 ± 20 K. The beam averaged column density is $2.0 \pm 0.5 \times 10^{18}$ cm^{-2}. The beam filling factor is 0.55 ± 0.10, indicating either a single compact structure in the beam or a clumpy structure filling the beam. Since CH_3OH is resolved (Fig. 5.2), the later interpretation is favored. We further estimate the fractional abundance of CH_3OH toward S255IR–SMA1 by taking the ratio of CH_3OH column density and H_2 column density derived from continuum emission (Sect. 5.3.1.2). We find that X[CH_3OH] is about 8×10^{-7}. In this estimate, we assume the derived H_2 column density is totally associated with the hot-core component ($V_{\rm LSR} \sim 4$ km s^{-1}). Therefore, the derived CH_3OH fractional abundance should be treated as a lower limit, and may be twice as high, assuming equal contributions from both velocity components. The high CH_3OH fractional abundance implies an active hot-core chemistry (e.g., Garrod et al. 2008). For other molecules, we estimate the total column densities and fractional abundances with the assumptions of optically thin emission, a single excitation temperature at 140 K and beam filling factor unity via Eq. 5.4. If the assumed excitation temperature has a factor of 2 in uncertainty, the derived column density has a factor of $\sim$ 2 in uncertainty. The optically thin assumption may not be valid if the peak intensity for a given molecule is similar to the one of CH_3OH. For a consistency check, we estimate the line center opacities of the observed lines via Eq. 5.5. We find that all observed lines do have moderate opacities (0.2–0.5) except CH_3OH which is optically thick ($\geq$1). Therefore, the derived molecular column densities are underestimated by 10%–30%. Results are summarized in Table 5.3.

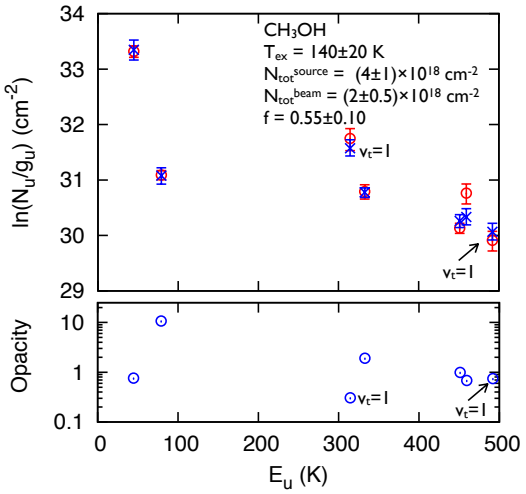

Figure 5.4 Population diagram analysis of the CH_3OH transitions. The red color represents the observed data, while the blue color represents the best-fit model. The estimated line center opacities are also shown in the bottom panel. See Sect. 5.3.2.2 for details.

Table 5.3. Molecular column density and fractional abundance

Molecule	N (cm^{-2})	$\tau_0{}^a$	X	Note
SO	5.4×10^{15}	0.3	2.2×10^{-9}	
SO_2	7.1×10^{16}	0.4	2.8×10^{-8}	
HCCCN	4.3×10^{14}	0.2	1.7×10^{-10}	
HCOOH	3.3×10^{16}	0.5	1.3×10^{-8}	
CH_3OH	2.0×10^{18}	≥ 1	8.0×10^{-7}	derived from PD
NH_2CHO	1.7×10^{15}	0.4	6.7×10^{-10}	

Note. — We assume an excitation temperature of 140 K in the estimation. The derived column density and fractional abundance should be treated as lower limits since non-negligible opacities are present. We only report the values for the blue-shifted component and we assume that the adopted H_2 column density (2.5×10^{24} cm^{-2}) refers to the blue-shifted component only. ^{a}Estimated line center opacity.

From the population diagram analysis outlined above, we found that the excitation temperature toward S255IR–SMA1 is about 140 K. The high H_2 volume density (3×10^9 cm^{-3}) derived from the continuum emission (Sect. 5.3.1.2) implies that collisions may dominate the excitation of CH_3OH and hence the the derived excitation temperature may be a good approximation of the true kinetic temperature of the source. To further investigate this issue, we adopted the non-LTE code RADEX in the large velocity gradient (LVG) regime (van der Tak et al. 2007) to model the observed CH_3OH lines. Limited by the collisional rate coefficients (Rabli & Flower 2010; Schöier et al. 2005), we only included the four A-type transitions in the calculations (Table 5.2). The free parameters in RADEX are kinetic temperature, H_2 volume density and CH_3OH column density. We fix a mean FWHM line width of 3.8 km s^{-1} in the calculations. Additionally, the beam filling factor is also taken into account for comparing with the observations. To find the excitation conditions, we performed χ^2 minimization in the 4-dimensional parameter space. The χ^2 distributions near the global minimum along each parameter axis are shown in Fig. 5.5. We found that the derived H_2 number density ($\geq 10^9$ cm^{-3}) is quite high and is comparable to the one estimated from the continuum emission. At such a high H_2 density, the level populations are likely thermalized (c.f., the critical density of CH_3OH is about 10^6–10^7 cm^{-3}). The derived kinetic temperature is similar to the excitation temperature obtained from the population diagram analysis. In addition, the derived CH_3OH column density and beam filling factor are similar to the solution derived from the population diagram analysis as well. We conclude that the level populations of CH_3OH are dominated by collisions with H_2 in S255IR–SMA1. A gas density of at least 10^9 cm^{-3} is present in a clumpy environment with a kinetic temperature of 140 K.

5.3.2.3 Kinematics

In Fig. 5.6, we show the gas kinematics traced by SO_2, HCOOH and CH_3OH. We observed velocity gradients roughly in the north-south direction, which is approximately perpendicular to the large scale jet-like CO outflow observed by Y. Wang et al. (2011). A similar velocity gradient in the north-south direction is also seen in CH_3CN and $HCOOCH_3$ lines at about $2''$ resolution (Y. Wang et al. 2011). Our sub-arcsecond resolution eSMA observations allow us to further obtain the kinematic information down to scales of few hundred AU. A clear velocity gradient traced by CH_3OH is seen, suggesting a rotating structure. In Fig. 5.7, we show the position-velocity (PV) maps of SO_2, HCOOH and CH_3OH. The PV cut is centered at the continuum peak position with P.A. 155°. The emission morphology in the PV maps does not follow Keplerian rotation. Rather, the signature is more like a linear velocity gradient. This observed gradient can be the result of two different motions: rigid-body rotation, or Keplerian-like rota-

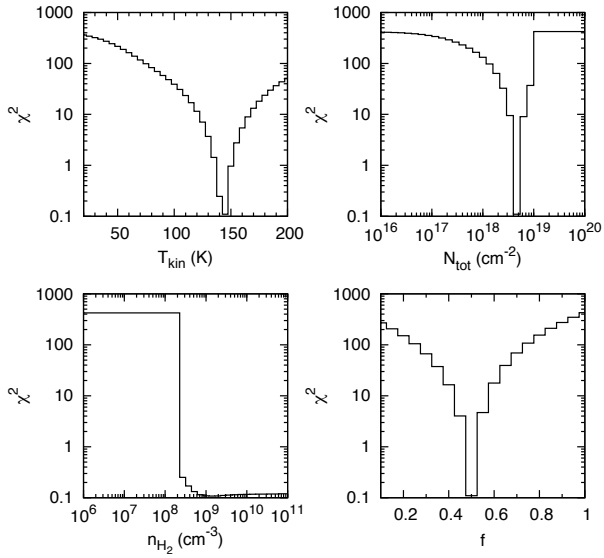

Figure 5.5 Excitation analysis of CH_3OH lines with the non-LTE code RADEX. The χ^2 distributions near the global minimum along each parameter axis are shown.

tion plus strong turbulence which smears out the "butterfly" signature of a pure Keplerian rotation. In addition, the observed spectra from the hot-core molecules (Fig. 5.2) are all single-peaked, not double-peaked as usually seen from a Keplerian rotating structure. We estimated the magnitude of the linear velocity gradient to be $0.8 - 2.3$ km s^{-1} per 100 AU, or $1.3 - 3.8$ km s^{-1} at a radius 165 AU (the geometric mean radius from continuum emission). From the spatial distribution of the CO outflow (Y. Wang et al. 2011) and water masers (Goddi et al. 2007), the rotating structure is not likely face-on. Assuming an disk inclined by $45°$, the Keplerian rotation speed at radius 165 AU is about 4.6 km s^{-1} for a stellar mass of 8 $M_\odot$. The observed velocity gradients imply that the stellar mass is only 0.6–5.5 $M_\odot$ if the rotation is Keplerian. From this analysis, we suggest that pure Keplerian rotation for a luminous massive source (2×10^4 $L_\odot$) does not fit our data. The observed rotating structure may have sub-Keplerian rotation and turbulence, or rigid-body rotation. Sensitive observations at at least $0.03''$ resolution may be helpful to resolve the kinematics.

We further study the kinematics traced by CH_3OH by adopting a toy model with the radiative transfer code RATRAN (Hogerheijde & van der Tak 2000). Due to the low S/N ratio of CH_3OH data, we only focus on the morphology of PV map and the line profile and perform a qualitative study. We assume a sphere with a diameter of 330 AU. The gas density and kinetic temperature profiles are cho-

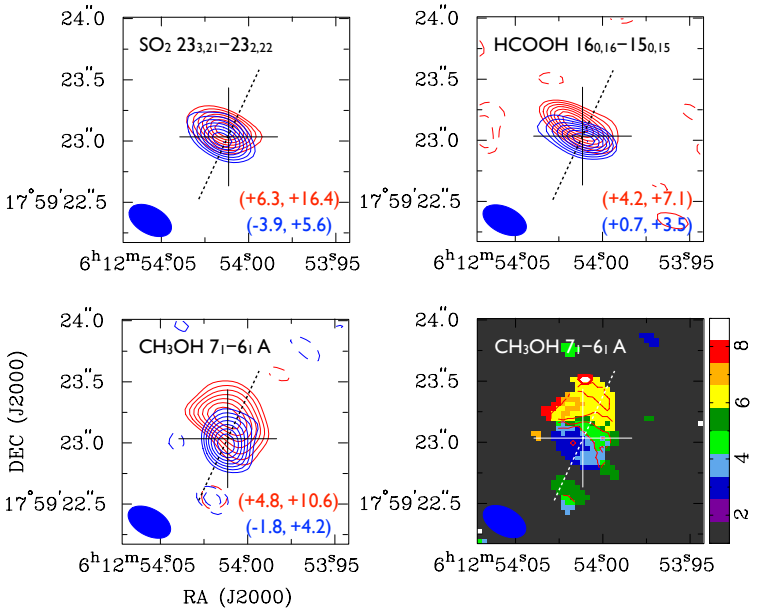

Figure 5.6 Kinematics of S255IR–SMA1 traced by SO_2 $23_{3,21}-23_{2,22}$, HCOOH $16_{0,16}-15_{0,15}$ and CH_3OH 7_1-6_1 A. Maps with blue and red contours are the the zero moment maps integrated over different velocity ranges as indicated on the plots. The first moment map of CH_3OH 7_1-6_1 A is plotted in color scale. The cross and the ellipse in each map represent the peak position of the continuum emission and the clean beam size, respectively. The dotted line represents the position-velocity cut at P.A. $155°$.

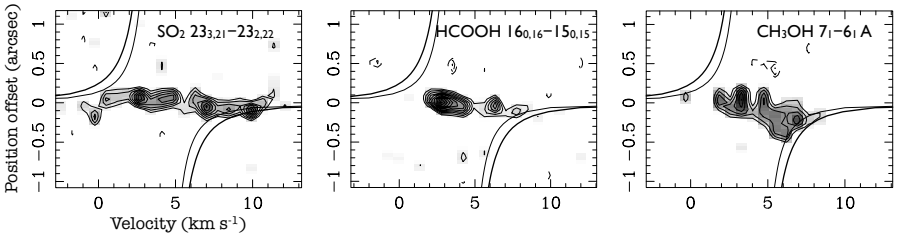

Figure 5.7 Position-velocity maps taken at the continuum peak with P.A. $155°$. The curves represent the projected ($45°$) Keplerian rotation velocities of a star with 14 $M_\odot$ (thick) and a star with 8 $M_\odot$ (thin). None of the observed position-velocity maps fits the Keplerian rotation.

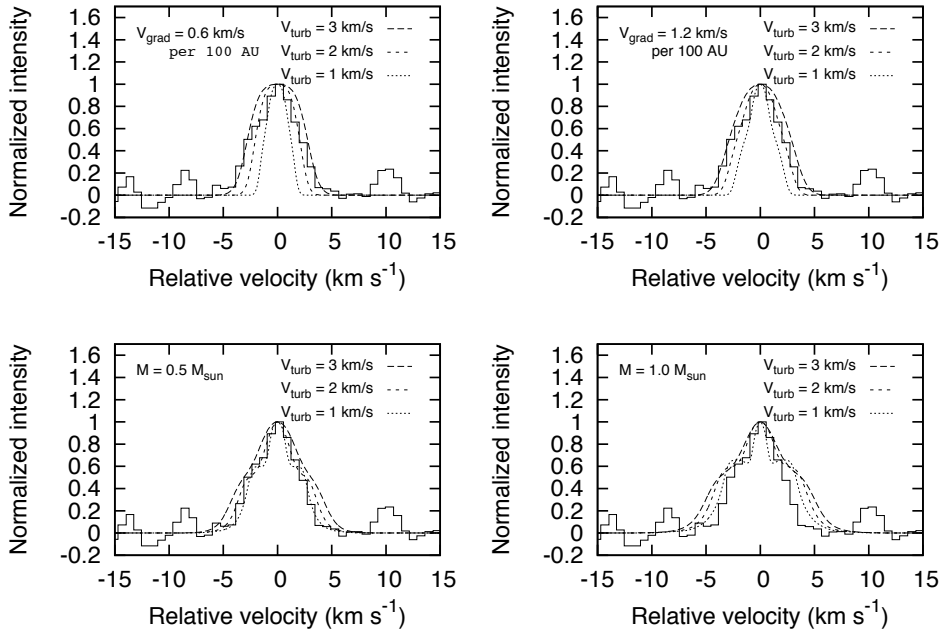

Figure 5.8 Toy models of kinematics. The upper panels are the rigid-body rotation models, while the bottom panels are the Keplerian models.

sen as $n(r) = 1.7 \times 10^9 (r/165\mathrm{AU})^{-1.5}$ cm^{-3} and $T(r) = 103(r/165\mathrm{AU})^{-0.4}$ K, respectively. The reference density is chosen such that the mean density is matched to the derived value from our 345-GHz continuum. The reference temperature is selected such that the mass-weighted temperature equals the kinetic temperature derived from the excitation analysis. Since the observed CH_3OH lines are optically thick, the fractional abundance of the test molecule is chosen to make the model line optically thick as well. We consider two different kinematics: Keplerian rotation and rigid-body rotation, in which stellar mass and the strength of the linear velocity gradient are the respective free parameters. In addition, the strength of turbulent FHWM line width is set as free parameter. We do not perform any parameter optimization, but rather focus on the general trend.

In Fig. 5.8, the rigid-body rotation models are shown in the upper panels, while the Keplerian models are presented in the bottom panels. The observed CH_3OH spectrum (averaged over a $0.8'' \times 0.8''$ region) is shown in solid lines. The observed CH_3OH line profile is single-peaked, rather than double-peaked. This fact sets a strong constraint on the stellar mass in the Keplerian models. As we demonstrate in Fig. 5.8 (bottom-right), a stellar mass of 1 $M_\odot$ generates too wide a line profile even if the turbulent line width is small. If we reduce the stellar mass to 0.5 $M_\odot$, the observed line profile can be modeled well with

turbulent FWHM line widths of 1–2 km s^{-1}. Based on our simple Keplerian toy models, we suggest that the observed rotating structure traced by CH_3OH is not in Keplerian rotation around a star of the expected mass of $\geq 8\ M_\odot$. The rotation may be strongly sub-Keplerian. In the rigid-body rotation models, we found that the line profiles are more sensitive to the adopted turbulent line width. Our results suggest that it is possible to model the kinematics traced by CH_3OH as rigid-body rotation with a typical turbulent line width of 2–3 km s^{-1}. Based our toy models, we cannot distinguish these two different kinematics in our data. Turbulence is important in shaping the line profiles.

5.4 Discussion

5.4.1 Luminosity, stellar mass, and accretion rate

The observed total luminosity ($L_{\rm total} \sim 2\times10^4 L_\odot$ at 1.6 kpc; Minier et al. 2005) sets an upper limit of the stellar mass of S255IR–SMA1 of about 16 $M_\odot$ by comparing with the luminosities of main-sequence stars (Mottram et al. 2011, and reference therein). The detection of an ultracompact HII region toward S255IR–SMA1 (Snell & Bally 1986) implies that the central powering source is more massive than about 8 $M_\odot$ which sets a lower limit of the stellar mass of S255IR–SMA1. This mass range ($8 < M_\star/M_\odot < 16$) suggests that S255IR–SMA1 is forming an early B-type star.

The 345-GHz continuum image allows us to estimate the core mass and H_2 volume density of S255IR–SMA1, which are 0.36 $M_\odot$ and 3.4×10^9 cm^{-3}, respectively (Sect. 5.3.1.2). Within the possible range of central stellar masses, the free-fall timescale,

$$t_{\rm ff} = \sqrt{\frac{3\pi}{32G\bar{\rho}}}, \tag{5.6}$$

where G is the gravitational constant and $\bar{\rho} = \frac{M_\star + M_{\rm core}}{4/3\pi R_{\rm core}^3}$ is the mean density of the core, is found to be 100 to 150 yrs for stellar mass between 8 and 16 $M_\odot$. We adopted $R_{\rm core} = 165$ AU as the geometric mean of the radii derived from the visibility fit (Table 5.1.) On 330 AU scales around S255IR–SMA1, we find that the free-fall accretion rate ($\dot{M} = M_{\rm core}/t_{\rm ff}$) is about $2-4\times10^{-3}\ M_\odot\ {\rm yr}^{-1}$, which set an upper limit of accretion rate if gas moves in slower than free fall. This derived high accretion rate implies a stellar accretion luminosity,

$$L_{\rm acc} = \frac{GM_\star\dot{M}}{R_\star} \tag{5.7}$$

of about $1 - 3 \times 10^5\ L_\odot$, where $R_\star$ is the stellar radius. In the above calculations, we adopted the main-sequence properties of stars at different stellar masses based on (Mottram et al. 2011, and reference therein). In Fig. 5.9, we plot the

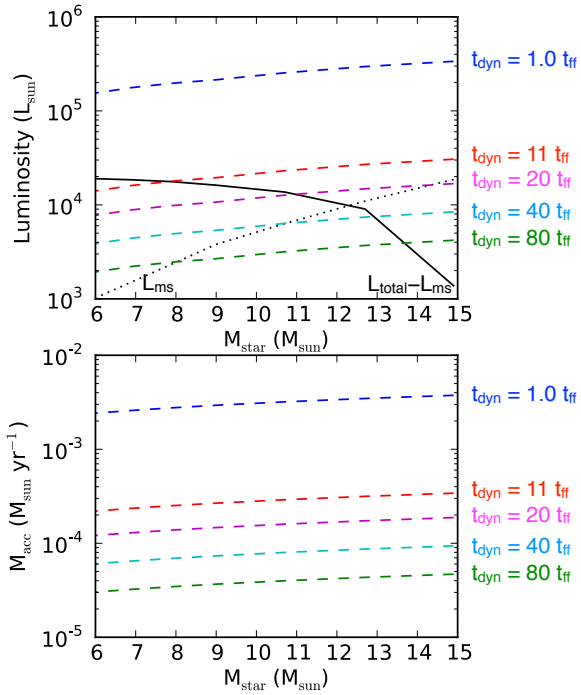

Figure 5.9 (Upper) Luminosity versus stellar mass. The main-sequence stellar luminosities taken from Mottram et al. (2011, and reference therein) are plotted in black dotted line, while the differences of the observed total luminosity and the main sequence luminosity are plotted in black solid line. The observed total luminosity sets an upper limit of the stellar mass to be about 20 $M_{\odot}$. The other dashed lines in different colors denote the accretion luminosities for different dynamical time scales. (Bottom) Accretion rate versus stellar mass plot. The dashed lines in different colors represent the derived accretion rates at different dynamic time scales.

luminosity and accretion rate versus stellar mass in the 8 to 16 $M_{\odot}$ range. We found that the derived stellar accretion luminosities exceed the observed total luminosity ($\sim 2 \times 10^4 L_{\odot}$), which implies that the central star does not obtain its mass via spherical free-fall accretion in one free-fall time.

In order to solve the above "luminosity problem", we suggest that the dynamic age ($t_{\rm dyn}$) of the source must be greater than one free-fall time. This will reduce the accretion rate and hence the accretion luminosity. We assume that the observed total luminosity can be simplified to the sum of the main-sequence luminosity and the accretion luminosity ($L_{\rm total} = L_{\rm ms} + L_{\rm acc}$). In the top panel of Fig. 5.9, we plot the difference between the observed total luminosity and the main-sequence luminosity ($L_{\rm total} - L_{\rm ms}$) in black. The accretion luminosities

with different dynamic timescales (11, 20, 40 and 80 free-fall times) are overplotted as color dashed lines. From this analysis, we suggest that the dynamic time scale of the source must be at least 11 free-fall time (about 1400 yrs) in order to match the minimum stellar mass of 8 $M_{\odot}$. The real dynamic timescale of the source requires a better estimate of the central stellar mass. In the bottom panel of Fig. 5.9 we also present the modified accretion rates at different dynamic ages. We note that the modified accretion rates are a few times 10^{-5} to a few times 10^{-4} $M_{\odot}$ yr^{-1}, which are typical values (Keto 2003) for massive star formation.

The derived minimum dynamic time scale (about 1400 yrs) implies that S255IR–SMA1 may be a very young forming early B-type star. Since S255IR–SMA1 cannot undergo free-fall collapse, we alternatively suggest that a disk may have been formed in order to help regulate the mass transport from the inner envelope to the star. Indeed, the velocity gradient seen in CH_3OH (Fig. 5.6) supports this idea. CH_3OH traces a rotating structure perpendicular to the optical jets (Howard et al. 1997; Miralles et al. 1997) and the alignment of water maser spots (Goddi et al. 2007). The non-unity beam filling factor derived from CH_3OH excitation analysis implies the rotating structure is likely clumpy, perhaps due to fragmentation. It is unclear what supports the observed rotating structure around SMA1 against collapse. As we demonstrate in Sect. 5.3.2.3, turbulence does play a role in shaping the line profile of a rotating structure. The non-Keplerian rotation may be due to the presence of a magnetic field (e.g., Seifried et al. 2011). To summarize, we propose that S255IR–SMA1 is a forming early B-type star surrounded by a rotating structure seen in CH_3OH. We suggest that the rotating structure is part of the inner envelope which covers both infalling and rotating gas components. There might be a true Keplerian disk close to the star with a size much less than 330 AU, which requires at least $0.03''$ resolution observations to properly resolve the kinematics.

5.4.2 Hot-core molecules in S255IR–SMA1: tracing forming massive star

It has been suggested that the hot core phase, during which complex organic molecules such CH_3OH, CH_3CN, $HCOOCH_3$, etc. can be observed, is one of the early stages of massive star formation (Zinnecker & Yorke 2007). Our eSMA observations toward S255IR–SMA1 show that hot core molecules trace massive star formation activity. We find two velocity components along the line of sight of S255IR–SMA1, of which only one component shows emission from hot core species. The derived high CH_3OH fractional abundance in the gas phase ($\sim 10^{-6}$) is an indication that the source has been heated recently. As a comparison, the gas-phase CH_3OH fractional abundance in dark clouds is a few times 10^{-8} (Ohishi et al. 1992). By comparing the derived fractional abundances of hot

core molecules with the gas-grain warm-up chemical models proposed by Garrod et al. (2008), we found that the chemical timescales are about $3 - 4 \times 10^4$, $1 - 2 \times 10^5$, and 7×10^5 yrs, depending on the warm-up speeds of star-forming core (respectively for models F, M, and S; Garrod et al. 2008). Based on the timescale estimated from the luminosity analysis presented in Sect. 5.4.1, we suggest that the heat up process in S255IR–SMA1 may be relatively fast (model F). However, the implied chemical timescale (few 10^4 yrs) from our data is about an order of magnitude greater than the minimum timescale derived from our luminosity analysis. We suggest that this is still in good agreement if we consider all the uncertainties of both approaches. Nevertheless, the presence of rich hot-core molecules toward S255IR–SMA1 suggests that the dynamic age of S255IR–SMA1 is only $\sim 10^{3-4}$ yrs.

5.5 Summary

We summarize our findings toward S255IR–SMA1 based on the subarcsecond resolution eSMA observations in the following:

(1) The continuum emission at 345 GHz toward S255IR–SMA1 is elongated in a direction roughly perpendicular to the NE-SW outflow, indicative of a disk-like structure.

(2) The inferred H_2 column density, mass, and volume density are 2.5×10^{24} cm^{-2}, 0.36 $M_\odot$, and 3.4×10^9 cm^{-3}, respectively. Our eSMA observations probe the innermost densest part of S255IR–SMA1.

(3) From the molecular line observations, two velocity components are identified, with one at $V_{\rm LSR} \sim 4$ km s^{-1} tracing the massive star formation activities of S255IR–SMA1, judging from the presence of hot-core molecules. The component at $V_{\rm LSR} \sim 9$ km s^{-1} may trace the common envelope of the binary system covering SMA1 and SMA2.

(4) Excitation analysis of CH_3OH lines suggests a mean temperature of 140 K and a mean volume density of 10^9 cm^{-3} for the inner dense parts of S255IR–SMA1.

(5) CH_3OH line shows a velocity gradient roughly perpendicular to the reported jet/outflow in the NE-SW direction. However, the PV map cannot be explained by pure-Keplerian rotation for the expected stellar mass of an early B-type star. It is likely that the observed structure is the inner part of the star-forming core undergoing infall and rotation. High-angular resolution observations at at least $0.03''$ in optically thin lines are required to reveal if there is a true Keplerian disk associated with S255IR–SMA1.

(6) The accretion rate is estimated to be a few times 10^{-5} to a few times 10^{-4} $M_{\odot}$ yr^{-1}. The dynamical age of S255IR–SMA1 is likely small (10^{3-4} yrs) based on the luminosity analysis in Sect. 5.4.1 and from the comparison of the derived CH_3OH abundance with chemical models.

Acknowledgements

We sincerely appreciate the strong support from Ray Blundell, Gary Davis, and Tom Phillips, the directors of the SMA, JCMT, and CSO, respectively, without whom the eSMA would not be possible. The eSMA project has been facilitated by grant 614.061.416 from the Netherlands Organisation for Scientific Research, NWO. The research of K.-S.W. at Leiden Observatory is supported through a PhD grant from the Nederlandse Onderzoekschool voor Astronomie (NOVA). This research has made use of NASA's Astrophysics Data System Bibliographic Services.

Bibliography

Beltrán, M. T., Cesaroni, R., Neri, R., & Codella, C. 2011, A&A, 525, A151

Beuther, H., Linz, H., & Henning, T. 2012, A&A, 543, A88

Beuther, H., Schilke, P., Sridharan, T. K., et al. 2002, A&A, 383, 892

Bonnell, I. A., Bate, M. R., Clarke, C. J., & Pringle, J. E. 2001, MNRAS, 323, 785

Bottinelli, S., Young, K. H., Chamberlin, R., et al. 2008, in Society of Photo-Optical Instrumentation Engineers (SPIE) Conference Series, Vol. 7012, Society of Photo-Optical Instrumentation Engineers (SPIE) Conference Series

Cesaroni, R., Galli, D., Lodato, G., Walmsley, C. M., & Zhang, Q. 2007, Protostars and Planets V, 197

Comito, C., Schilke, P., Endesfelder, U., Jiménez-Serra, I., & Martín-Pintado, J. 2007, A&A, 469, 207

Furuya, R. S., Cesaroni, R., Takahashi, S., et al. 2008, ApJ, 673, 363

Garrod, R. T., Weaver, S. L. W., & Herbst, E. 2008, ApJ, 682, 283

Goddi, C., Moscadelli, L., Sanna, A., Cesaroni, R., & Minier, V. 2007, A&A, 461, 1027

Goldsmith, P. F. & Langer, W. D. 1999, ApJ, 517, 209

Hildebrand, R. H. 1983, QJRAS, 24, 267

Hogerheijde, M. R. & van der Tak, F. F. S. 2000, A&A, 362, 697

Howard, E. M., Pipher, J. L., & Forrest, W. J. 1997, ApJ, 481, 327

Jaffe, D. T., Davidson, J. A., Dragovan, M., & Hildebrand, R. H. 1984, ApJ, 284, 637

Keto, E. 2003, ApJ, 599, 1196

Kraus, S., Hofmann, K.-H., Menten, K. M., et al. 2010, Nature, 466, 339

McKee, C. F. & Tan, J. C. 2003, ApJ, 585, 850

Mezger, P. G., Chini, R., Kreysa, E., Wink, J. E., & Salter, C. J. 1988, A&A, 191, 44

Minier, V., Burton, M. G., Hill, T., et al. 2005, A&A, 429, 945

Miralles, M. P., Salas, L., Cruz-Gonzalez, I., & Kurtz, S. 1997, ApJ, 488, 749

Mottram, J. C., Hoare, M. G., Davies, B., et al. 2011, ApJ, 730, L33

Müller, H. S. P., Schlöder, F., Stutzki, J., & Winnewisser, G. 2005, Journal of Molecular Structure, 742, 215
Ohishi, M., Irvine, W. M., & Kaifu, N. 1992, in IAU Symposium, Vol. 150, Astrochemistry of Cosmic Phenomena, ed. P. D. Singh, 171
Ojha, D. K., Samal, M. R., Pandey, A. K., et al. 2011, ApJ, 738, 156
Ossenkopf, V. & Henning, T. 1994, A&A, 291, 943
Pickett, H. M., Poynter, R. L., Cohen, E. A., et al. 1998, J. Quant. Spec. Radiat. Transf., 60, 883
Pillai, T., Kauffmann, J., Wyrowski, F., et al. 2011, A&A, 530, A118
Rabli, D. & Flower, D. R. 2010, MNRAS, 406, 95
Rengarajan, T. N. & Ho, P. T. P. 1996, ApJ, 465, 363
Rygl, K. L. J., Brunthaler, A., Reid, M. J., et al. 2010, A&A, 511, A2
Sánchez-Monge, Á., Cesaroni, R., Beltrán, M. T., et al. 2013, A&A, 552, L10
Sault, R. J., Teuben, P. J., & Wright, M. C. H. 1995, in Astronomical Society of the Pacific Conference Series, Vol. 77, Astronomical Data Analysis Software and Systems IV, ed. R. A. Shaw, H. E. Payne, & J. J. E. Hayes, 433
Schöier, F. L., van der Tak, F. F. S., van Dishoeck, E. F., & Black, J. H. 2005, A&A, 432, 369
Scoville, N. Z., Carlstrom, J. E., Chandler, C. J., et al. 1993, PASP, 105, 1482
Seifried, D., Banerjee, R., Klessen, R. S., Duffin, D., & Pudritz, R. E. 2011, MNRAS, 417, 1054
Sharpless, S. 1959, ApJS, 4, 257
Shu, F. H., Adams, F. C., & Lizano, S. 1987, ARA&A, 25, 23
Simpson, J. P., Burton, M. G., Colgan, S. W. J., et al. 2009, ApJ, 700, 1488
Snell, R. L. & Bally, J. 1986, ApJ, 303, 683
Tamura, M., Gatley, I., Joyce, R. R., et al. 1991, ApJ, 378, 611
van der Tak, F. F. S., Black, J. H., Schöier, F. L., Jansen, D. J., & van Dishoeck, E. F. 2007, A&A, 468, 627
Y. Wang, Y., Beuther, H., Bik, A., et al. 2011, A&A, 527, A32
Zhang, Q., Hunter, T. R., Brand, J., et al. 2001, ApJ, 552, L167
Zinchenko, I., Liu, S.-Y., Su, Y.-N., et al. 2012, ApJ, 755, 177
Zinnecker, H. & Yorke, H. W. 2007, ARA&A, 45, 481